Elucidating the Intrinsic Activity and Selectivity of Cu for Nitrate Electroreduction

Zhuanghe Ren,[1] Kaige Shi,[1] and Xiaofeng Feng[1,2,3,4]*

[1]Department of Physics, University of Central Florida, Orlando, Florida 32816, United States

[2]Renewable Energy and Chemical Transformations (REACT) Cluster, University of Central Florida, Orlando, Florida 32816, United States

[3]Department of Chemistry, University of Central Florida, Orlando, Florida 32816, United States

[4]Department of Materials Science and Engineering, University of Central Florida, Orlando, Florida 32816, United States

*Email: Xiaofeng.Feng@ucf.edu (X.F.)

ABSTRACT:

Cu-based catalysts have been widely explored for the electrochemical nitrate reduction reaction (NO_3RR), while the intrinsic activity and selectivity of Cu metal for NO_3RR remain ambiguous, preventing a genuine comparison of the NO_3RR performance. Here we use polycrystalline Cu foils for benchmarking and elucidate the impact of often overlooked factors on the NO_3RR, including Cu facet exposure, nitrate concentration, and electrode surface area. An electropolished Cu foil exhibits a higher activity and selectivity for NO_3RR to NH_3 than a wet-etched Cu foil, benefiting from greater exposure of Cu(100) facets that are more favorable for the NO_3RR. While the NH_3 selectivity shows no apparent dependence on the nitrate concentration, it increases monotonically with Cu electrode area, which is attributed to a promoted conversion of intermediately produced NO_2^- to NH_3 on a larger electrode, as validated by ^{15}N isotope labeling experiment. Our work provides mechanistic insights towards the rational design of NO_3RR electrocatalysts.

The electrochemical reduction of nitrate (NO_3^-) has recently received considerable interest because of its potential for the denitrification of wastewater as well as the sustainable production of ammonia (NH_3).[1] The use of nitrogen fertilizers has contributed significantly to the growth of agricultural production, but the nitrogen use efficiency is typically lower than 40%,[2] so that most of the nitrogen leaches into groundwater, lakes, and rivers, causing nitrate contamination in the groundwater and surface water. Nitrate is also widely distributed in industrial wastewater.[3] The rising concentration of nitrate has caused severe environmental problems such as eutrophication and disturbance of ecosystems.[4] The electrochemical reduction of nitrate has recently emerged as a promising route for the removal of NO_3^- from wastewater,[5,6] as it can be powered by solar- or wind-generated electricity with NH_3 as a major product. Therefore, the nitrate reduction reaction (NO_3RR) can also enable a sustainable route for NH_3 production, as an alternative to the energy- and carbon-intensive Haber–Bosch process.[7–9]

The electrochemical reduction of NO_3^- to NH_3 is a complex process involving the transfer of eight electrons and consecutive hydrogenation and deoxygenation steps: $NO_3^- + 6H_2O + 8e^- \rightarrow NH_3 + 9OH^-$. Meanwhile, the electroreduction of NO_3^- also forms other side products such as NO_2^- and N_2,[5] so the design of NO_3RR catalysts typically aims at a high selectivity for NH_3 production. In addition, a relatively high overpotential is needed to drive the reaction so that the hydrogen evolution reaction (HER) becomes competitive and thus lowers the Faradaic efficiency for the NO_3RR. As a result, a high concentration of NO_3^- was often employed in the electrolyte because more hydrogen adsorbed on an electrode surface can participate in the NO_3RR instead of the HER.[10–12] However, typical nitrate sources such as industrial wastewater and polluted ground water, have a low NO_3^- concentration ranging from few to few tens of mM,[13,14] which limits the availability of nitrate-rich streams for the NO_3RR electrolysis. Therefore, those relatively HER-inert catalysts have received much attention for the NO_3RR, including Cu-, Co-, Ti-, modified Ru- and carbon-based materials and single-atom catalysts.[15–28]

Among the various candidates, Cu-based catalysts are of particular interest for the NO_3RR, due to their relatively high activity and selectivity for NH_3 production and low cost.[29,30] Many strategies have been used to design Cu-based materials to enhance the NO_3RR performance, such as forming Cu nanostructures, heterostructures, alloys and molecular catalysts.[31–42] For example, Ru-dispersed Cu nanorods were developed, which achieved a current density of 1 A cm^{-2} for the NO_3RR with a high NH_3 Faradaic efficiency of 93%,[39] greatly promoting the practical viability of the NO_3RR electrolysis. Despite the progress of Cu-based electrocatalysts for the NO_3RR, the understanding of the activity and selectivity of metallic Cu for the NO_3RR remains ambiguous, as reflected by the various NO_3RR performance reported in the literature.[17,33,34,36,39,40] In addition, nitrite (NO_2^-) plays a distinctively dual role in the NO_3RR, which is a side product as well as a key intermediate towards NH_3 production.[23] The concentration, diffusion, and reaction of the intermediately produced NO_2^- can strongly impact the measured NO_3RR selectivity,[43,44] while the

unique role of NO_2^- in the NO_3RR catalysis remains to be elucidated. Therefore, understanding the intrinsic activity and selectivity of Cu for the NO_3RR is essential to achieve a benchmarking and a consistent picture of the NO_3RR catalytic performance for rational catalyst design.[44]

In this work, we use high-purity polycrystalline Cu foils as a model catalyst and benchmark electrode to investigate the intrinsic activity and selectivity of Cu for the NO_3RR. Particularly, we focus on the impact of often overlooked factors on the NO_3RR performance, including Cu facet exposure, nitrate concentration, and electrode area.[44] For Cu foils cleaned by two commonly used pre-treatment methods (wet etching and electropolishing), we find that the electropolished Cu foil exhibits a higher activity and selectivity for NH_3 production as compared to the wet-etched Cu foil, which originates from the pre-treatment induced different exposures of Cu facets. Moreover, the NH_3 selectivity increases monotonically with Cu electrode surface area, and such a dependence is attributed to a promoted NO_2^- conversion to NH_3 on a larger electrode, as validated by ^{15}N isotope labeling experiment. The understandings are further applied to prepare a modified Cu foil electrode with increased Cu(100) facets and surface area, which achieves a ~50% increase in the NO_3RR activity as compared to the electropolished Cu foil with a NH_3 Faradaic efficiency of 91% at −0.2 V vs the reversible hydrogen electrode (RHE).

Commercial Cu foils with an ultrahigh purity of 99.9999% were used throughout this work to minimize possible influence of impurities and to understand the intrinsic activity of Cu. Prior to electrocatalytic measurements, a pre-treatment is required to remove surface contaminants on a Cu foil, such as organic residues and native oxides. There are two common cleaning methods: wet etching and electropolishing,[29,34,36,39] so we cleaned Cu foils using the two methods, respectively (see the Experimental Methods in the Supporting Information for details), and the derived samples are referred to as "wet-etched" and "electropolished" Cu foils. The cleaned Cu foil electrodes were evaluated for the NO_3RR in a two-compartment electrochemical cell (H-cell) under well-defined mass transport conditions for the study of intrinsic kinetics. A 1 M KOH electrolyte containing 5 mM KNO_3 was used, based on typical NO_3^- concentrations in wastewater sources.[28,45] Linear sweep voltammetry (LSV) was first performed to evaluate the electrokinetics of NO_3RR. As shown in Figure 1a, the current density on the electropolished Cu foil increased rapidly as the potential shifted from 0.15 to −0.35 V vs RHE and then reached a mass-transport-limited plateau at more negative potentials. In comparison, the current density on the wet-etched Cu foil showed a similar potential dependence from 0.15 to −0.35 V, but was much lower than that on the electropolished Cu foil at the same potential, indicating a lower activity of the wet-etched sample. Both LSV curves showed two reduction peaks at around 0.08 and −0.15 V, which can be attributed to NO_3^- reduction to NO_2^- and further reduction to NH_3, respectively.[29,32] In addition, LSV curves were recorded in 1 M KOH electrolyte (no NO_3^-) as blank experiment, as exhibited in Figure S1, where the HER current densities only started to increase rapidly at potentials < −0.4 V vs RHE. Therefore, the HER had a negligible contribution to the measured activity in the LSV curves in

Figure 1a, so the reduction peaks should be from the NO_3RR. The difference between the two LSV curves may be attributed to the pre-treatment induced exposure of Cu facets with different NO_3RR activities,[32,38] as will be discussed later.

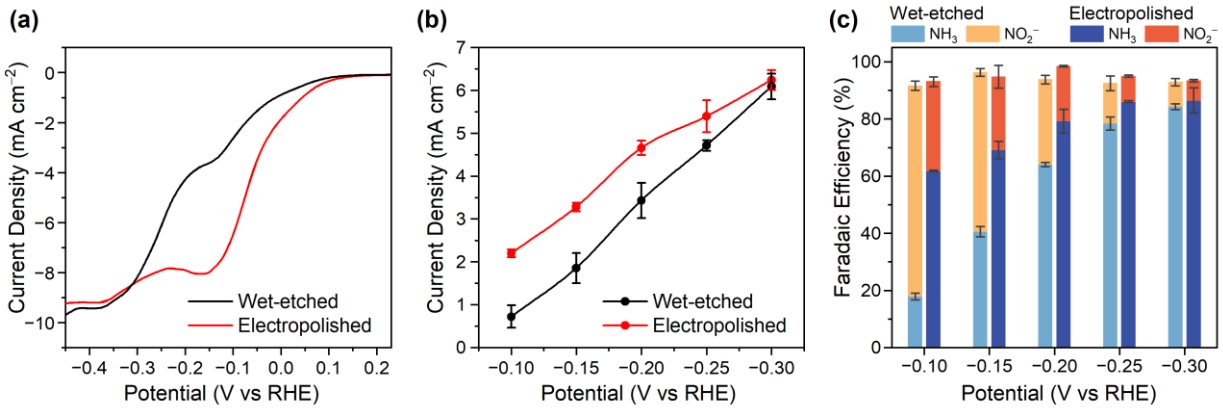

Figure 1. Evaluation of the NO_3RR performance on the Cu foils with different pre-treatments. (a) LSV curves recorded on the wet-etched and electropolished Cu foils in 1 M KOH + 5 mM KNO_3 electrolyte. Scan rate = 5 mV s^{-1}. (b) Current densities and (c) corresponding Faradaic efficiencies for the bulk electrolysis on the two Cu foils in 1 M KOH + 5 mM KNO_3 electrolyte at selected potentials. The error bars represent the standard deviation of three independent measurements.

Bulk electrolysis was then performed at potentials ranging from −0.1 to −0.3 V vs RHE to quantify the NO_3RR products and compare the selectivity between the two Cu foil samples, with a typical electrolysis time of 30 min. Two products, NH_3 and NO_2^-, were identified in the catholyte and quantified by the indophenol blue method and the Griess method, respectively,[46,47] based on the calibration curves in Figures S2 and S3. Gas-phase product of the electrolysis was examined by gas chromatography, and no H_2 or N_2 was detected in the potential window. As shown in Figure 1b, the current density on the electropolished Cu foil increased from 2.2 to 6.2 mA cm^{-2} as the potential shifted from −0.1 to −0.3 V, while the wet-etched sample showed an apparently smaller current density, particularly at low overpotentials (−0.1 to −0.2 V), consistent with the LSV data. The Faradaic efficiency for NH_3 production also had a similar difference between the two Cu foils. As shown in Figure 1c, the NH_3 Faradaic efficiency on the electropolished Cu foil increased from 62% to 87% as the potential shifted from −0.1 to −0.3 V, with the opposite trend for the NO_2^- Faradaic efficiency that decreased from 31% to 7% along with the potential shift. In contrast, the wet-etched Cu foil exhibited a NH_3 Faradaic efficiency increasing from 18% to 78% and a NO_2^- Faradaic efficiency decreasing from 74% to 14% along with the potential shift from −0.1 to −0.25 V, indicating an apparently lower NO_3RR activity and NH_3 selectivity on the wet-etched Cu foil than that on the electropolished Cu foil.

To unveil the origin of different NO_3RR performances on the two Cu foils, we characterized their morphology, chemical state, and surface structure. As exhibited in Figure S4, the scanning electron microscopy (SEM) image of the pristine Cu foil (without pre-treatment) showed that the foil surface was generally flat. After the wet-etching treatment, the Cu foil was similarly flat with some white areas (SEM images in Figures 2a, S5a), which may be caused by some residue copper oxides from the etching process. In comparison, the electropolished Cu foil had a highly smooth surface at both small and large scales (Figures 2b, S5b), which remained unchanged after 30-min bulk electrolysis test (Figure S6). The comparison of morphology excludes the influence of surface roughness on the NO_3RR performance as the wet-etched Cu foil had a slightly rougher surface yet a lower activity, and vice versa for the electropolished Cu foil. X-ray photoelectron spectroscopy (XPS) was then performed to examine the chemical state of Cu in the samples. The Cu 2p spectra of the pristine Cu foil in Figure 2c showed only doublet and satellite peaks corresponding to Cu^{2+},[48] indicating a high coverage of CuO on the foil surface due to the oxidation by air. After either pre-treatment, the CuO was mostly removed from the foil surfaces, as indicated by the major peaks of Cu^0 and very minor peaks of Cu^{2+} (Figure 2c). Meanwhile, Cu LMM Auger spectra were acquired to analyze the chemical state of the outermost surface.[49] As shown in Figure 2d, both Cu foil surfaces were dominated by Cu^0 with a small fraction of Cu^{2+} after the pre-treatments, indicating that the chemical state was identical for the two Cu foils and could not account for the NO_3RR performance difference.

Furthermore, the surface structure of the Cu foils was analyzed using the electrosorption of OH as a probe (see the Experimental Methods in the Supporting Information for details).[17] As shown in Figure 2e, the electropolished Cu foil showed a much higher (100) adsorption peak in the cyclic voltammetry (CV) curve than that on the wet-etched foil, whereas the (111) peaks had similar intensities, indicating a greater exposure of Cu(100) facets on the electropolished foil. It was reported that the Cu(100) surface was more favorable for the NO_3RR than the Cu(111) surface,[32,38] as the Cu(100) facets facilitate the initial $*NO_3$ adsorption and first hydrogenation step and thus promote the entire NO_3RR.[50] It thus well explains the different NO_3RR performances on the two Cu foils and the higher activity of the electropolished Cu foil with more Cu(100) facets exposed. Such a surface structure dependence should also account for the different peak intensities in the LSV curves (Figure 1a).[32] Such sensitivity of the NO_3RR activity to metal facets was also observed on Pd catalysts,[20] which may indicate a general structure-sensitive nature of the NO_3RR catalysis.

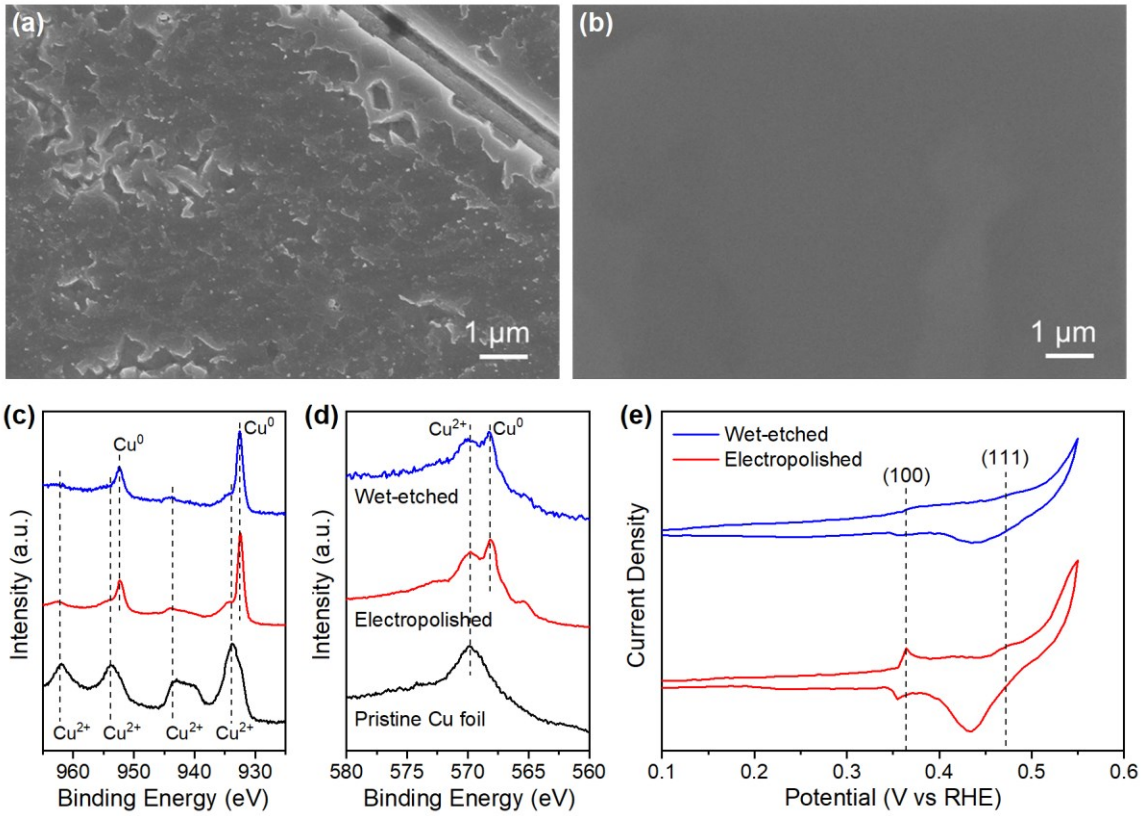

Figure 2. Characterizations of the two Cu foils with different pre-treatments. (a–b) SEM images of the (a) wet-etched and (b) electropolished Cu foils. (c) Cu 2p XPS and (d) Cu LMM Auger spectra of the pristine and pre-treated Cu foils. (e) CV curves recorded on the two Cu foils in 1 M KOH electrolyte for the OH electrosorption tests. Scan rate = 100 mV s^{-1}.

Based on the above results, the electropolished Cu foil with a higher activity was selected as the "standard" Cu foil sample for further investigations below. As the NO_3^- concentration was reported to influence the NO_3RR selectivity,[33,43,44] such as a higher concentration leading to an increased N_2 production or a suppressed HER,[43] we evaluated the NO_3RR on the electropolished Cu foil in 1 M KOH electrolytes containing various concentrations of NO_3^-. As shown in Figure 3a, the current density of the bulk electrolysis on the Cu foil at −0.2 V vs RHE increased linearly from 4.7 to 47.3 mA cm^{-2} as the NO_3^- concentration increased from 5 to 50 mM. Plot of the natural logarithm of the NO_3RR current density vs the natural logarithm of the NO_3^- concentration (Figure S7) indicates that it is a first-order reaction. Meanwhile, the Faradaic efficiencies remained almost constant at around 79% and 19% for the production of NH_3 and NO_2^-, respectively, as shown in Figure 3b. Therefore, the NO_3RR selectivity showed no apparent dependence on the initial NO_3^- concentration, at least in the case of flat Cu foil electrodes and relatively low NO_3^- concentrations, where the influence of electrode morphology and possible N-N coupling to form N_2 is negligible. This may reflect the intrinsic selectivity of Cu for the NO_3RR.

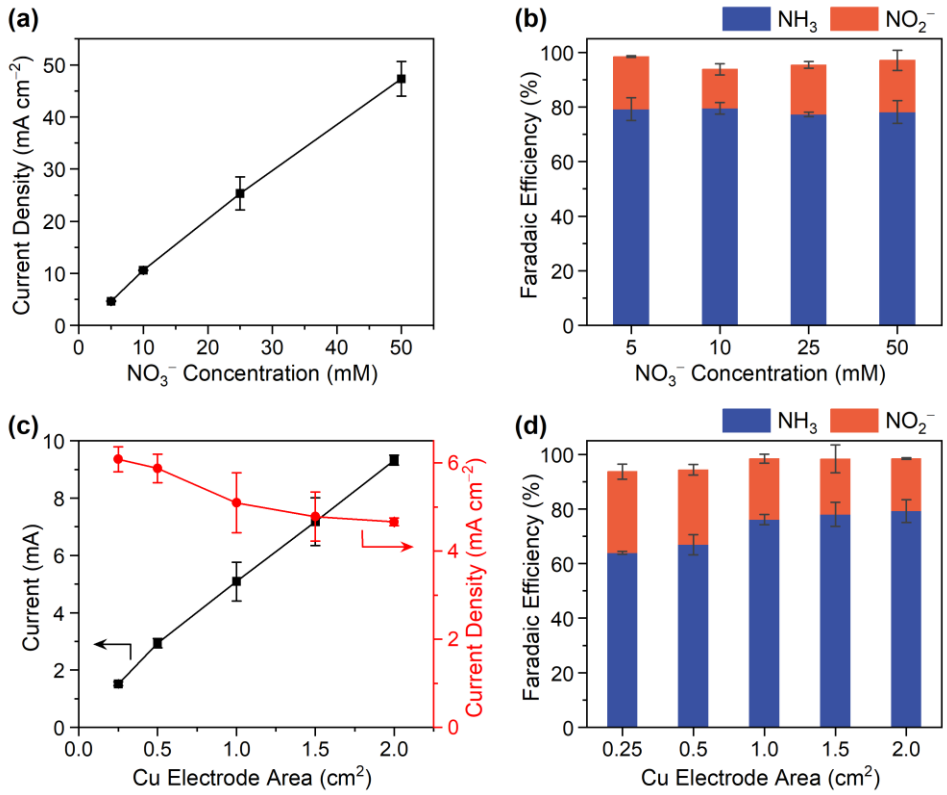

Figure 3. Dependence of the NO_3RR performance on the NO_3^- concentration and Cu electrode area. (a) Current densities and (b) Faradaic efficiencies for the NO_3RR on the electropolished Cu foil in 1 M KOH electrolytes containing different concentrations of NO_3^- at −0.2 V vs RHE. (c) Current densities and (d) Faradaic efficiencies for the NO_3RR on the electropolished Cu foils with different surface areas in 1 M KOH + 5 mM KNO_3 electrolyte at −0.2 V vs RHE. The error bars represent the standard deviation of three independent measurements.

We further examined the role of Cu electrode area in the NO_3RR catalysis, as nanostructured electrodes with high surface areas were often used in previous studies, while the surface area was not considered to correlate with the NO_3RR selectivity. Here we varied the Cu foil surface area from 0.25 to 2 cm^2, and the electrolysis current on the Cu foil increased almost linearly from 1.5 to 9.3 mA under typical test conditions (5 mM NO_3^-, −0.2 V vs RHE), as shown in Figure 3c. Meanwhile, the electrode-area-normalized current density decreased slightly from 6.1 to 4.7 mA cm^{-2}, which is attributed to the higher current that caused a faster drop of the NO_3^- concentration during the test with a larger Cu electrode in the H-cell. Unexpectedly, the Faradaic efficiency for NH_3 production gradually increased from 64% to 79% along with the increase of the Cu electrode area from 0.25 to 2.0 cm^2, as shown in Figure 3d. We postulate that the dependence of the NO_3RR selectivity on the electrode area arises from the difference and evolution of the NO_2^- concentration in the catholyte. The higher current on a larger Cu electrode resulted in a higher concentration of

NO_2^-, which was further reduced to NH_3 and thus increased the total production of NH_3 over the electrolysis time (30 min) and the NH_3 Faradaic efficiency counted over the duration.

As the intermediately produced NO_2^- continues to act as a reactant together with remaining NO_3^-, the actual reactant during an electrolysis is a mixture of NO_2^- and NO_3^-. Thus, we quantified the concentrations of NO_2^- and NO_3^- in the electrolyte and derived their ratios at different times of bulk electrolysis, as shown in Figure 4a. Interestingly, although $c(NO_2^-)/c(NO_3^-)$ was evolving with time, the ratios were largely the same at each time between the cases of 5 and 50 mM NO_3^- (due to the linear nature of first-order reaction kinetics), but distinct for the electrodes of different areas (0.25 vs 2 cm^2). The same trend of $c(NO_2^-)/c(NO_3^-)$ during the electrolysis of 5 and 50 mM NO_3^- should explain their similar NH_3 Faradaic efficiencies. In contrast, a lower $c(NO_2^-)/c(NO_3^-)$ for the electrode of 0.25 cm^2 area means that there is less NO_2^- (relative to NO_3^-) to be reduced to NH_3, leading to a lower Faradaic efficiency for overall NH_3 production. Thus, $c(NO_2^-)/c(NO_3^-)$ may play an important role in determining the NH_3 selectivity, as the reduction of intermediately produced NO_2^- to NH_3 can increase the total NH_3 Faradaic efficiency. This conclusion should be generally applicable to the cases of flat electrodes and low NO_3^- concentrations, where the mass transport of NO_3^-/NO_2^- is not influenced by electrode morphology and the N-N coupling to form N_2 is negligible.

The above analysis raised the question whether the reduction of intermediately produced NO_2^- competes with and influences the reduction of remaining NO_3^-. To clarify the relationship between the reduction of NO_3^- and NO_2^-, ^{15}N isotope labeling experiment was performed in 1 M KOH electrolytes containing 5 mM $^{15}NO_3^-$ and various concentrations of $^{14}NO_2^-$ (0−5 mM). The reaction products were distinguished and quantified by ^1H nuclear magnetic resonance (NMR) spectroscopy based on the calibration curves in Figure S8. As expected, the current density for the reduction of $^{14}NO_2^-$ gradually increased along with the increase of the $^{14}NO_2^-$ concentration, as shown in Figure 4b. Meanwhile, the current density for the reduction of $^{15}NO_3^-$ remained nearly unchanged, indicating a negligible competition between the reduction of NO_3^- and NO_2^-, at least at the low concentrations. Consistently, the Faradaic efficiency of the $^{15}NO_3RR$ remained constant, around 77% for $^{15}NH_3$ production, which was not influenced by the added $^{14}NO_2^-$ (Figure 4c). In contrast, the total Faradaic efficiency for ammonia production from both $^{15}NO_3^-$ and $^{14}NO_2^-$ increased from 77% to 85% as the $^{14}NO_2^-$ concentration increased from 0 to 5 mM, as shown in Figure 4c, benefiting from a nearly 100% selectivity for $^{14}NO_2^-$ reduction to NH_3. Therefore, the isotope labeling experiment indicates that the reduction of intermediately produced NO_2^- does not compete with the reduction of NO_3^-, but contributes to the total production of NH_3. This explains the higher Faradaic efficiency for NH_3 production on larger Cu electrodes (Figure 3d), where more NO_2^- was produced and subsequently reduced to NH_3, elevating the overall NH_3 selectivity.

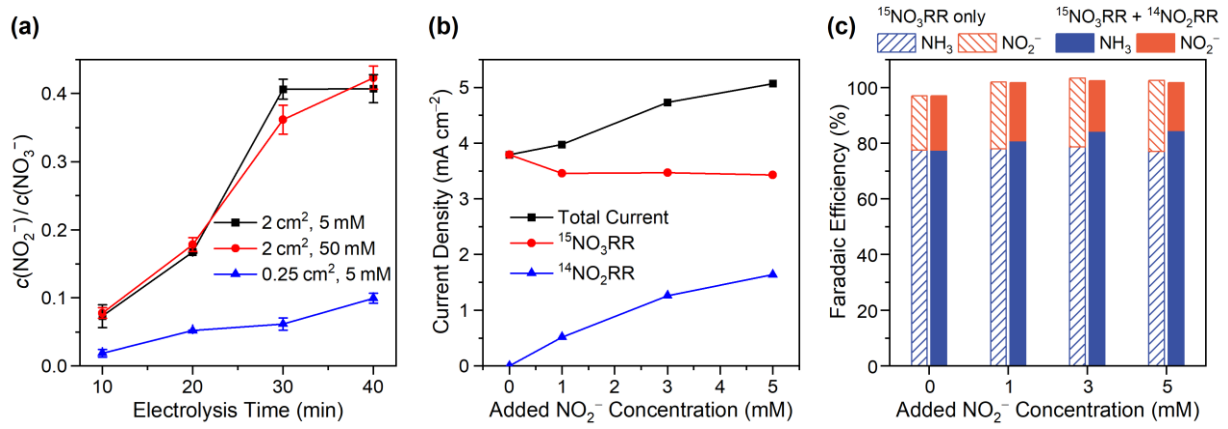

Figure 4. Effect of the presence of NO_2^- on the NH_3 selectivity. (a) Ratio of the concentrations of NO_2^- and NO_3^- in the electrolyte at different times of bulk electrolysis on the electropolished Cu foils at −0.2 V vs RHE. The error bars represent the standard deviation of three independent measurements. (b–c) ^{15}N isotope labelling experiment: (b) current densities and (c) corresponding Faradaic efficiencies for the bulk electrolysis at −0.2 V vs RHE in 1 M KOH electrolyte containing 5 mM $^{15}NO_3^-$ and different concentrations of $^{14}NO_2^-$. $^{15}NO_3RR$ represents all products originating from $^{15}NO_3^-$, and $^{14}NO_2RR$ represents the products from $^{14}NO_2^-$, as distinguished and quantified by NMR spectroscopy.

To further examine the above understandings, we applied them to prepare a modified Cu foil electrode by forming Cu nanocubes on a Cu foil, thus to increase Cu(100) facets and surface area and demonstrate their enhancement of the NO_3RR activity and selectivity. As previously reported, Cu nanocubes could be prepared by initial formation of Cu_2O nanocubes using a metal ion cycling method,[51] followed by electrochemical reduction of Cu_2O to Cu (see the Experimental Methods in the Supporting Information for details). The SEM image in Figure 5a showed that the Cu foil surface was fully covered by nanocubes with smooth surfaces after the Cu^{2+} cycling process. The morphology of the sample remained similar after the subsequent electroreduction step, as shown in Figure 5b, despite the presence of some cracks between areas. Grazing-incidence XRD patterns of the samples confirmed that Cu_2O was first grown on the Cu foil surface after the Cu^{2+} cycling process and then converted to metallic Cu by the electroreduction step (Figure 5c). The surface of the Cu nanocubes sample was dominated by (100) facets, as revealed by the OH electrosorption test in Figure 5d.[17] The derived sample is hereafter referred to as the "Cu nanocubes" sample.

The Cu nanocubes sample was evaluated for the NO_3RR at selected potentials in 1 M KOH electrolyte containing 5 mM NO_3^-. As shown in Figure 5e, the current density on the Cu nanocubes sample increased from 3.9 to 7.3 mA cm^{-2} as the potential shifted from −0.1 to −0.25 V vs RHE, which was roughly 50% higher than that on the electropolished Cu foil in the potential window, demonstrating a greatly enhanced NO_3RR activity of the Cu nanocubes. The Faradaic efficiency

for NH_3 production on the Cu nanocubes sample exhibited a similar trend (Figure 5f) and gradually increased from 77% to 91% as the potential shifted from −0.1 to −0.25 V, which was higher by 5−15% than that on the electropolished Cu foil at the potentials. Therefore, both NO_3RR activity and NH_3 selectivity were considerably improved for the NO_3RR on the Cu nanocubes sample, confirming the effects of Cu(100) facets and electrode surface area on the NO_3RR and providing guidance for the rational design of NO_3RR catalysts.

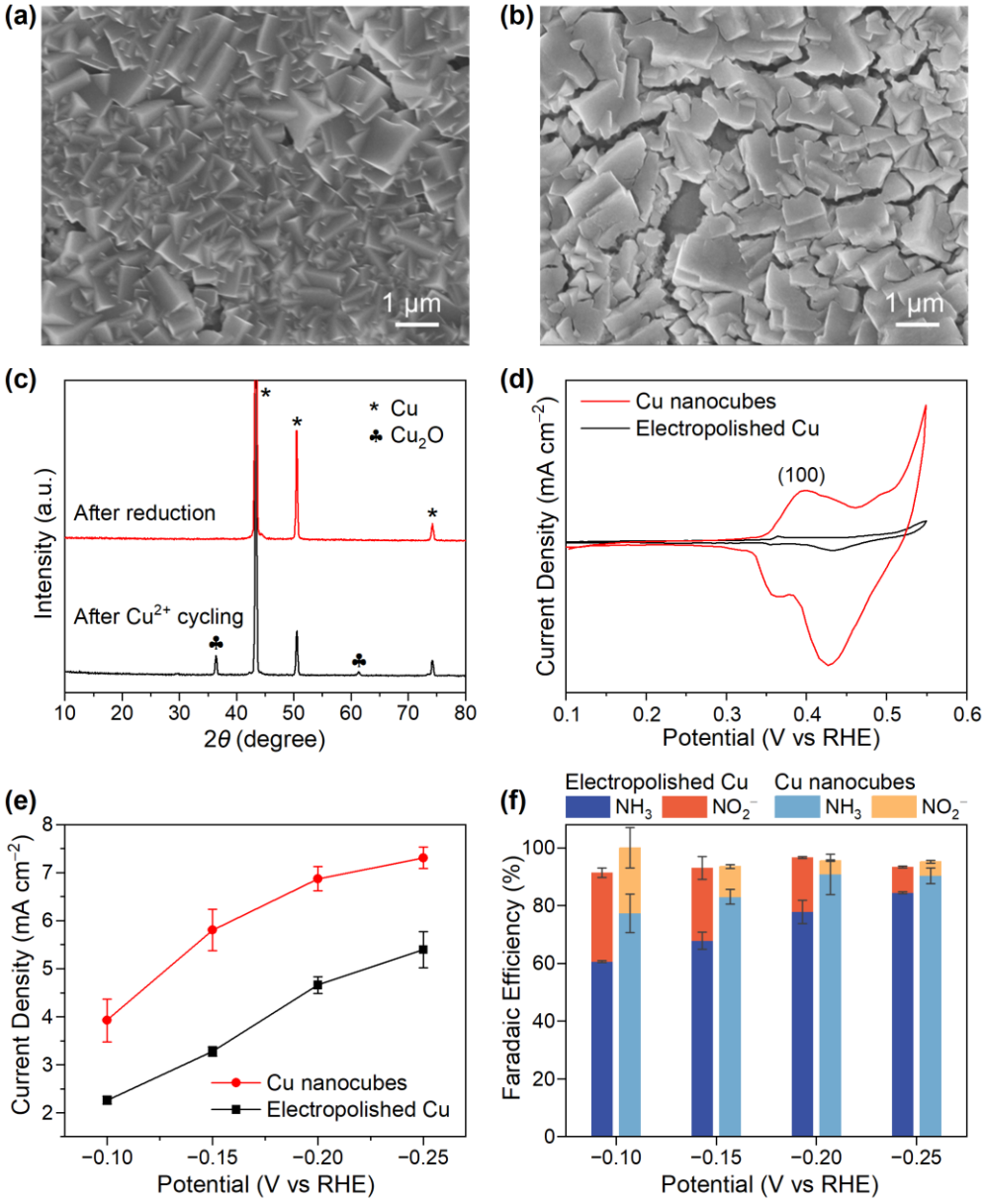

Figure 5. Characterization and electrocatalytic performance of the Cu nanocubes sample for the NO_3RR. (a−b) SEM images of the sample (a) after Cu^{2+} cycling treatment and (b) after further electroreduction. (c) Grazing-incidence XRD patterns of the sample after Cu^{2+} cycling and after

reduction. (d) CV curves recorded on the Cu nanocubes and the electropolished Cu foil samples in 1 M KOH electrolyte for OH electrosorption tests. Scan rate = 100 mV s^{-1}. (e) Current densities and (f) Faradaic efficiencies for NO_3RR on the Cu nanocubes and electropolished Cu foil samples in 1 M KOH + 5 mM KNO_3 electrolyte at selected potentials. The error bars represent the standard deviation of three independent measurements.

In summary, we investigated the intrinsic activity and selectivity of Cu for the NO_3RR using polycrystalline Cu foils for benchmarking and revealed the effects of often overlooked factors on the NO_3RR performance. For Cu foils cleaned by different pre-treatments, the electropolished Cu foil exhibited an apparently higher activity and selectivity for NH_3 production than the wet-etched Cu foil, due to greater exposure of Cu(100) facets that are more favorable for the NO_3RR. While the NH_3 selectivity showed no apparent dependence on the NO_3^- concentration, it increased monotonically with the Cu electrode area, which was attributed to a promoted NO_2^- conversion to NH_3 as a result of a higher concentration of intermediately produced NO_2^- in the catholyte with a larger electrode. The understandings were further applied to prepare a modified Cu foil electrode with increased Cu(100) facets and surface area, which enhanced the NO_3RR activity by ~50% with a NH_3 Faradaic efficiency of 91% at −0.2 V vs RHE. Our work not only elucidated the important but often overlooked factors on the NO_3RR performance, but also provided mechanistic insights into the intrinsic activity and selectivity towards the rational design of NO_3RR electrocatalysts.

ASSOCIATED CONTENT

Supporting Information.

The Supporting Information is available free of charge at …

Experimental methods, additional materials characterization and electrochemical measurements (Figures S1−S8) (PDF)

AUTHOR INFORMATION

Corresponding Author

*E-mail: Xiaofeng.Feng@ucf.edu

ORCID: Zhuanghe Ren: 0000-0002-0858-2987
Kaige Shi: 0000-0003-1372-0210
Xiaofeng Feng: 0000-0002-9473-2848

Notes: The authors declare no competing financial interest.

ACKNOWLEDGMENTS

This material is based upon work supported by the National Science Foundation (NSF) under Grant No. 1943732. Z.R. acknowledges the support from the Preeminent Postdoctoral Program (P3) at the University of Central Florida. The authors acknowledge the use of an XPS instrument supported by the NSF MRI: ECCS: 1726636.

REFERENCES

(1) Zeng, Y.; Priest, C.; Wang, G.; Wu, G. Restoring the nitrogen cycle by electrochemical reduction of nitrate: progress and prospects. *Small Methods* **2020**, *4*, 2000672.

(2) Canfield, D. E.; Glazer, A. N.; Falkowski, P. G. The evolution and future of Earth's nitrogen cycle. *Science* **2010**, *330*, 192−196.

(3) Choudhary, M.; Muduli, M.; Ray, S. A comprehensive review on nitrate pollution and its remediation: conventional and recent approaches. *Sustain. Water Resour. Manag.* **2022**, *8*, 113.

(4) Galloway, J. N.; Townsend, A. R.; Erisman, J. W.; Bekunda, M.; Cai, Z.; Freney, J. R.; Martinelli, L. A.; Seitzinger, S. P.; Sutton, M. A. Transformation of the nitrogen cycle: recent trends, questions, and potential solutions. *Science* **2008**, *320*, 889−892.

(5) Wang, Y.; Wang, C.; Li, M.; Yu, Y.; Zhang, B. Nitrate electroreduction: mechanism insight, in situ characterization, performance evaluation, and challenges. *Chem. Soc. Rev.* **2021**, *50*, 6720−6733.

(6) Yang, X.; Mukherjee, S.; O'Carroll, T.; Hou, Y.; Singh, M. R.; Gauthier, J. A.; Wu, G. Achievements, challenges, and perspectives on nitrogen electrochemistry for carbon-neutral energy technologies. *Angew. Chem. Int. Ed.* **2023**, *62*, e202215938.

(7) Lim, J.; Fernández, C. A.; Lee, S. W.; Hatzell, M. C. Ammonia and nitric acid demands for fertilizer use in 2050. *ACS Energy Lett.* **2021**, *6*, 3676−3685.

(8) van Langevelde, P. H.; Katsounaros, I.; Koper, M. T. M. Electrocatalytic nitrate reduction for sustainable ammonia production. *Joule* **2021**, *5*, 290−294.

(9) Hu, L.; Pillai, H. S.; Feit, C.; Shi, K.; Gao, Z.; Banerjee, P.; Xin, H.; Feng, X. Identification of active sites for ammonia electrosynthesis on ruthenium. *ACS Energy Lett.* **2022**, *7*, 4290−4298.

(10) McEnaney, J. M.; Blair, S. J.; Nielander, A. C.; Schwalbe, J. A.; Koshy, D. M.; Cargnello, M.; Jaramillo, T. F. Electrolyte engineering for efficient electrochemical nitrate reduction to ammonia on a titanium electrode. *ACS Sustain. Chem. Eng.* **2020**, *8*, 2672−2681.

(11) Li, P.; Jin, Z.; Fang, Z.; Yu, G. A single-site iron catalyst with preoccupied active centers that achieves selective ammonia electrosynthesis from nitrate. *Energy Environ. Sci.* **2021**, *14*, 3522−3531.

(12) Wu, Z. Y.; Karamad, M.; Yong, X.; Huang, Q.; Cullen, D. A.; Zhu, P.; Xia, C.; Xiao, Q.; Shakouri, M.; Chen, F. Y.; et al. Electrochemical ammonia synthesis via nitrate reduction on Fe single atom catalyst. *Nat. Commun.* **2021**, *12*, 2870.

(13) Nguyen, T. T. P.; Do, B. K. D.; Bui, N. N.; Pham, M. A.; Nguyen, T. B. Selectiveness of copper and polypyrrole modified copper electrodes for nitrate electroreduction: a comparative study and application in ground water. *ECS Trans.* **2013**, *53*, 41−52.

(14) Chauhan, R.; Srivastava, V. C. Electrochemical denitrification of highly contaminated actual nitrate wastewater by Ti/RuO_2 anode and iron cathode. *Chem. Eng. J.* **2020**, *386*, 122065.

(15) Zhang, X.; Wang, Y.; Liu, C.; Yu, Y.; Lu, S.; Zhang, B. Recent advances in non-noble metal electrocatalysts for nitrate reduction. *Chem. Eng. J.* **2021**, *403*, 126269.

(16) Liu, J. X.; Richards, D.; Singh, N.; Goldsmith, B. R. Activity and selectivity trends in electrocatalytic nitrate reduction on transition metals. *ACS Catal.* **2019**, *9*, 7052−7064.

(17) Fu, X.; Zhao, X.; Hu, X.; He, K.; Yu, Y.; Li, T.; Tu, Q.; Qian, X.; Yue, Q.; Wasielewski, M. R.; Kang, Y. Alternative route for electrochemical ammonia synthesis by reduction of nitrate on copper nanosheets. *Appl. Mater. Today* **2020**, *19*, 100620.

(18) Jia, R.; Wang, Y.; Wang, C.; Ling, Y.; Yu, Y.; Zhang, B. Boosting selective nitrate electroreduction to ammonium by constructing oxygen vacancies in TiO_2. *ACS Catal.* **2020**, *10*, 3533−3540.

(19) Yu, Y.; Wang, C.; Yu, Y.; Wang, Y.; Zhang, B. Promoting selective electroreduction of nitrates to ammonia over electron-deficient Co modulated by rectifying Schottky contacts. *Sci. China Chem.* **2020**, *63*, 1469−1476.

(20) Lim, J.; Liu, C. Y.; Park, J.; Liu, Y. H.; Senftle, T. P.; Lee, S. W.; Hatzell, M. C. Structure sensitivity of Pd facets for enhanced electrochemical nitrate reduction to ammonia. *ACS Catal.* **2021**, *11*, 7568−7577.

(21) Liu, H.; Park, J.; Chen, Y.; Qiu, Y.; Cheng, Y.; Srivastava, K.; Gu, S.; Shanks, B. H.; Roling, L. T.; Li, W. Electrocatalytic nitrate reduction on oxide-derived silver with tunable selectivity to nitrite and ammonia. *ACS Catal.* **2021**, *11*, 8431−8442.

(22) Harmon, N. J.; Rooney, C. L.; Tao, Z.; Shang, B.; Raychaudhuri, N.; Choi, C.; Li, H.; Wang, H. Intrinsic catalytic activity of carbon nanotubes for electrochemical nitrate reduction. *ACS Catal.* **2022**, *12*, 9135−9142.

(23) Murphy, E.; Liu, Y.; Matanovic, I.; Guo, S.; Tieu, P.; Huang, Y.; Ly, A.; Das, S.; Zenyuk,

I.; Pan, X.; et al. Highly durable and selective Fe- and Mo-Based atomically dispersed electrocatalysts for nitrate reduction to ammonia via distinct and synergized NO_2^- pathways. *ACS Catal.* **2022**, *12*, 6651−6662.

(24) Zhang, J.; He, W.; Quast, T.; Junqueira, J. R. C.; Saddeler, S.; Schulz, S.; Schuhmann, W. Single-entity electrochemistry unveils dynamic transformation during tandem catalysis of Cu_2O and Co_3O_4 for converting NO_3^- to NH_3. *Angew. Chem. Int. Ed.* **2022**, *62*, e202214830.

(25) He, W.; Zhang, J.; Dieckhöfer, S.; Varhade, S.; Brix, A. C.; Lielpetere, A.; Seisel, S.; Junqueira, J. R. C.; Schuhmann, W. Splicing the active phases of copper/cobalt-based catalysts achieves high-rate tandem electroreduction of nitrate to ammonia. *Nat. Commun.* **2022**, *13*, 1129.

(26) Han, S.; Li, H.; Li, T.; Chen, F.; Yang, R.; Yu, Y.; Zhang, B. Ultralow overpotential nitrate reduction to ammonia via a three-step relay mechanism. *Nat. Catal.* **2023**, *6*, 402−414.

(27) Li, B.; Xia, F.; Liu, Y.; Tan, H.; Gao, S.; Kaelin, J.; Liu, Y.; Lu, K.; Marks, T. J.; Cheng, Y. $Co_2Mo_6S_8$ catalyzes nearly exclusive electrochemical nitrate conversion to ammonia with enzyme-like activity. *Nano Lett.* **2023**, *23*, 1459−1466.

(28) Wang, X.; Wu, X.; Ma, W.; Zhou, X.; Zhang, S.; Huang, D.; Winter, L. R.; Kim, J. H.; Elimelech, M. Free-standing membrane incorporating single-atom catalysts for ultrafast electroreduction of low-concentration nitrate. *Proc. Natl. Acad. Sci. U.S.A.* **2023**, *120*, e2217703120.

(29) Sang, E. B.; Karen, L. S.; Andrew, A. G. Nitrate adsorption and reduction on Cu(100) in acidic solution. *J. Am. Chem. Soc.* **2007**, *129*, 10171−10180.

(30) Reyter, D.; Bélanger, D.; Roué, L. Study of the electroreduction of nitrate on copper in alkaline solution. *Electrochim. Acta* **2008**, *53*, 5977−5984.

(31) Mattarozzi, L.; Cattarin, S.; Comisso, N.; Gambirasi, A.; Guerriero, P.; Musiani, M.; Vázquez-Gómez, L.; Verlato, E. Hydrogen evolution assisted electrodeposition of porous Cu-Ni alloy electrodes and their use for nitrate reduction in alkali. *Electrochim. Acta* **2014**, *140*, 337−344.

(32) Pérez-Gallent, E.; Figueiredo, M. C.; Katsounaros, I.; Koper, M. T. M. Electrocatalytic reduction of Nitrate on Copper single crystals in acidic and alkaline solutions. *Electrochim. Acta* **2017**, *227*, 77−84.

(33) Wang, Y.; Xu, A.; Wang, Z.; Huang, L.; Li, J.; Li, F.; Wicks, J.; Luo, M.; Nam, D. H.; Tan, C. S.; et al. Enhanced nitrate-to-ammonia activity on copper-nickel alloys via tuning of intermediate adsorption. *J. Am. Chem. Soc.* **2020**, *142*, 5702−5708.

(34) Wang, Y.; Zhou, W.; Jia, R.; Yu, Y.; Zhang, B. Unveiling the activity origin of a copper-

based electrocatalyst for selective nitrate reduction to ammonia. *Angew. Chem. Int. Ed.* **2020**, *59*, 5350−5354.

(35) Chen, G. F.; Yuan, Y.; Jiang, H.; Ren, S. Y.; Ding, L. X.; Ma, L.; Wu, T.; Lu, J.; Wang, H. Electrochemical reduction of nitrate to ammonia via direct eight-electron transfer using a copper–molecular solid catalyst. *Nat. Energy* **2020**, *5*, 605−613.

(36) Yuan, J.; Xing, Z.; Tang, Y.; Liu, C. Tuning the oxidation state of Cu electrodes for selective electrosynthesis of ammonia from nitrate. *ACS Appl. Mater. Interfaces* **2021**, *13*, 52469−52478.

(37) Hu, T.; Wang, C.; Wang, M.; Li, C. M.; Guo, C. Theoretical insights into superior nitrate reduction to ammonia performance of copper catalysts. *ACS Catal.* **2021**, *11*, 14417−14427.

(38) Wang, Y.; Qin, X.; Shao, M. First-principles mechanistic study on nitrate reduction reactions on copper surfaces: Effects of crystal facets and pH. *J. Catal.* **2021**, *400*, 62−70.

(39) Chen, F. Y.; Wu, Z. Y.; Gupta, S.; Rivera, D. J.; Lambeets, S. V.; Pecaut, S.; Kim, J. Y. T.; Zhu, P.; Finfrock, Y. Z.; Meira, D. M.; et al. Efficient conversion of low-concentration nitrate sources into ammonia on a Ru-dispersed Cu nanowire electrocatalyst. *Nat. Nanotechnol.* **2022**, *17*, 759−767.

(40) Gao, Q.; Pillai, H. S.; Huang, Y.; Liu, S.; Mu, Q.; Han, X.; Yan, Z.; Zhou, H.; He, Q.; Xin, H.; Zhu, H. Breaking adsorption-energy scaling limitations of electrocatalytic nitrate reduction on intermetallic CuPd nanocubes by machine-learned insights. *Nat. Commun.* **2022**, *13*, 338.

(41) Paliwal, A.; Bandas, C. D.; Thornburg, E. S.; Haasch, R. T.; Gewirth, A. A. Enhanced nitrate reduction activity from Cu-alloy electrodes in an alkaline electrolyte. *ACS Catal.* **2023**, *13*, 6754−6762.

(42) Zhou, N.; Wang, Z.; Zhang, N.; Bao, D.; Zhong, H.; Zhang, X. Potential-induced synthesis and structural identification of oxide-derived Cu electrocatalysts for selective nitrate reduction to ammonia. *ACS Catal.* **2023**, *13*, 7529−7537.

(43) Katsounaros, I.; Kyriacou, G. Influence of nitrate concentration on its electrochemical reduction on tin cathode: identification of reaction intermediates. *Electrochim. Acta* **2008**, *53*, 5477−5484.

(44) Barrera, L.; Silcox, R.; Giammalvo, K.; Brower, E.; Isip, E.; Bala Chandran, R. Combined effects of concentration, pH, and polycrystalline copper surfaces on electrocatalytic nitrate-to-ammonia activity and selectivity. *ACS Catal.* **2023**, *13*, 4178−4192.

(45) Ascott, M. J.; Gooddy, D. C.; Wang, L.; Stuart, M. E.; Lewis, M. A.; Ward, R. S.; Binley, A. M. Global patterns of nitrate storage in the vadose zone. *Nat. Commun.* **2017**, *8*, 1416.

(46) Searle, P. L. The Berthelot or indophenol reaction and its use in the analytical chemistry of

nitrogen. *Analyst* **1984**, *109*, 549−568.

(47) Green, L. C.; Wagner, D. A.; Glogowski, J.; Skipper, P. L.; Wishnok, J. S.; Tannenbaum, S. R. Analysis of nitrate, nitrite, and [^{15}N] nitrate in biological fluids. *Anal. Biochem.* **1982**, *126*, 131−138.

(48) Larson, P. E. X-ray induced photoelectron and auger spectra of Cu, CuO, Cu_2O, and Cu_2S thin films. *J. Electron Spectrosc. Relat. Phenom.* **1974**, *4*, 213−218.

(49) Platzman, I.; Brener, R.; Haick, H.; Tannenbaum, R. Oxidation of polycrystalline copper thin films at ambient conditions. *J. Phys. Chem. C* **2008**, *112*, 1101−1108.

(50) Fu, Y.; Wang, S.; Wang, Y.; Wei, P.; Shao, J.; Liu, T.; Wang, G.; Bao, X. Enhancing electrochemical nitrate reduction to ammonia over Cu nanosheets via facet tandem catalysis. *Angew. Chem. Int. Ed.* **2023**, *62*, e202303327.

(51) Jiang, K.; Sandberg, R. B.; Akey, A. J.; Liu, X.; Bell, D. C.; Nørskov, J. K.; Chan, K.; Wang, H. Metal ion cycling of Cu foil for selective C−C coupling in electrochemical CO_2 reduction. *Nat. Catal.* **2018**, *1*, 111−119.

Table of Contents (TOC) Graphic: